

Nuclear body movement is determined by chromatin accessibility and dynamics

Sabine M. Görisch*, Malte Wachsmuth†, Carina Ittrich‡, Christian P. Bacher§, Karsten Rippe*†, and Peter Lichter*¶

Divisions of *Molecular Genetics, †Intelligent Bioinformatics Systems, and ‡Biostatistics, Deutsches Krebsforschungszentrum, Im Neuenheimer Feld 280, D-69120 Heidelberg, Germany; and §AG Molekulare Biophysik, Kirchhoff-Institut für Physik, Im Neuenheimer Feld 227, D-69120 Heidelberg, Germany

Edited by Joseph G. Gall, Carnegie Institution of Washington, Baltimore, MD, and approved June 24, 2004 (received for review April 27, 2004)

Promyelocytic leukemia (PML) and Cajal bodies are mobile sub-nuclear organelles, which are involved in activities like RNA processing, transcriptional regulation, and antiviral defense. A key parameter in understanding their biological functions is their mobility. The diffusion properties of PML and Cajal bodies were compared with a biochemically inactive body formed by aggregates of murine Mx1 by using single-particle tracking methods. The artificial Mx1-yellow fluorescent protein body showed a very similar mobility compared with PML and Cajal bodies. The data are described quantitatively by a mechanism of nuclear body movement consisting of two components: diffusion of the body within a chromatin corral and its translocation resulting from chromatin diffusion. This finding suggests that the body mobility reflects the dynamics and accessibility of the chromatin environment, which might target bodies to specific nuclear subcompartments where they exert their biological function.

Cajal and promyelocytic leukemia (PML) bodies are essential components of the nucleus that are thought to contain activities for RNA processing, transcriptional regulation, and antiviral defense. For understanding their biological functions, parameters have to be identified that characterize their mobility and lead to a localization of Cajal and PML bodies at their target sites in the nucleus. Whereas Cajal bodies are often found associated to several different small nuclear RNA and small nucleolar RNA gene loci as well as histone gene loci (1–5), PML bodies are frequently located in the MHC gene region (6). For both nuclear bodies, different types of movements were described and assigned to distinct subgroups of Cajal and PML bodies (7–12). The analysis of a baby hamster kidney cell line revealed that a fraction of PML bodies moved over longer distances and in an energy-dependent manner. These faster moving bodies were not observed in HeLa cells (8). In a detailed study of Cajal bodies in HeLa cells, an anomalous diffusion behavior and an ATP- and transcription-dependent association with chromatin was reported (7).

Here, the mobility of PML and Cajal bodies has been compared with the nuclear body-like structures formed by Mx1 protein fused to yellow fluorescent protein (YFP). Mx proteins are IFN-induced GTPases of the dynamin super family involved in defense mechanisms against RNA viruses (13). The murine Mx1 protein, 72 kDa in size, has a natural nuclear localization sequence and displays a nuclear body-like distribution (14, 15). In contrast to the Mx1 WT protein, the Mx1-YFP construct studied has no antiviral activity as tested with influenza and Thogoto virus infection and formed crystals (S. Stertz and O. Haller, personal communication). The diffusion properties of this bona fide biologically inert body were used as a reference to identify principles determining the mobility of bodies within the nucleus.

Materials and Methods

Expression Plasmids. The cDNA coding for Mx1 in the plasmid pBS-T7 (kindly provided by O. Haller, University of Freiburg, Freiburg, Germany) was cut out and inserted into the pEYFP-C1 vector (Clontech) by using *Apal* and *Bam*H I. Expression plasmids coilin-GFP and GFP-PML-III (16) were kindly provided by C. Cardoso (Max Delbrück Center, Berlin) and A. Möller (University

of Bern, Bern, Switzerland), respectively. A SW13 cell line stably expressing H2A-cyan fluorescent protein (CFP) (SW13^{H2A-CFP}) was provided by M. Reichenzeller and T. A. Knoch (Deutsches Krebsforschungszentrum, Heidelberg).

Cell Culture and Transfection. HeLa cells (ATCC CCL-2) were cultured on 12-mm glass coverslips for immunofluorescence or 35-mm glass coverslips (Helmut Sauer, Reutlingen, Germany) and in Lab-Tek chambers (Nunc) for *in vivo* studies in DMEM for 1 day after plating. Cells were transiently transfected in duplicate or triplicate by using FuGENE 6 (Roche Diagnostics), as it was not possible to obtain a stable cell line with the Mx1-YFP crystals. The experiments were repeated with different batches of transfected cells, and the same results for all three types of nuclear bodies were obtained within the accuracy of the measurements. This finding indicates that when using transiently transfected cells reproducible expression levels were achieved, and that these cells were appropriate for studying nuclear mobility. For energy depletion sodium azide was added either to the medium to a final concentration of 10 mM or in a depletion buffer according to ref. 17. For *in vivo* staining of the DNA, the cells were incubated with 1 μ g/ml Hoechst 33342 (Molecular Probes) for 20 min.

Fixation and Indirect Immunofluorescence. After transfection, cells were incubated for 1–2 days and then fixed in 4% formaldehyde containing 2% sucrose on ice. For indirect immunofluorescence, cells were permeabilized with 0.2% Triton X-100 in PBS. To identify nuclear bodies the following mouse mAbs were used: anti-p80 coilin (kind gift of A. Lamond, University of Dundee, Dundee, U.K.), anti-fibrillarin (kind gift of D. Olins, Bowdoin College, New Brunswick, ME), and anti-PML PG-M3 (Santa Cruz Biotechnology). Secondary Texas red-conjugated antibodies (Dianova, Hamburg, Germany) were diluted 1:200. All coverslips were mounted by using VECTASHIELD with 4',6-diamidino-2-phenylindole (Vector Laboratories).

Confocal Laser Scanning and Correlative Electron Microscopy. 3D image stacks were acquired by using the Leica TCS SP2 confocal laser scanning microscope (Leica Microsystems, Mannheim, Germany). A diode laser as well as argon and helium/neon lasers were used for 4',6-diamidino-2-phenylindole/Hoechst ($\lambda = 405$ nm), GFP ($\lambda = 488$ nm), YFP ($\lambda = 514$ nm), and Texas red ($\lambda = 543$ nm) excitation. For all images a PlanApochromat $\times 63/1.32$ numerical aperture oil objective was used. For 4D imaging, cells were cultured by using DMEM without phenol red in a humid incubation chamber (Helmut Sauer) with temperature and CO₂ control (Pec-Con, Erbach, Germany). Either 45 or 98 stacks of 9–12 sections with 0.3- μ m *z* interval were collected every 10 s. Laser intensities were adjusted such that the power in the sample did not exceed 10 μ W, resulting in an energy deposition of ≈ 20 μ J per stack for the

This paper was submitted directly (Track II) to the PNAS office.

Abbreviations: *D*, diffusion coefficient; MSD, mean square displacement; PML, promyelocytic leukemia; YFP, yellow fluorescent protein; CFP, cyan fluorescent protein.

¶To whom correspondence should be addressed. E-mail: m.macleod@dkfz.de.

© 2004 by The National Academy of Sciences of the USA

selected scan speed (800 Hz) and image size (256×256 pixels) similar to the illumination energy deposition in previous studies (7, 8). Single Mx1-YFP bodies were bleached by using maximum laser intensity, and recovery was monitored every 5–10 min. For 4D imaging of cells with Mx1-YFP and H2A-CFP a Zeiss LSM 510 equipped with argon and krypton lasers for CFP ($\lambda = 413$ nm) and YFP ($\lambda = 514$ nm) as well as a PlanApochromat $\times 63/1.4$ numerical aperture oil differential interference contrast objective (Zeiss) was used. For all images 45 stacks with $0.5\text{-}\mu\text{m}$ z interval were recorded every 10 s. Maximum intensity projections were made with Leica confocal software and a Zeiss image browser. The method for correlative confocal laser scanning microscopy and electron microscopy investigation of Mx1-YFP was essentially as described (18).

Image Processing and Movement Analysis. Confocal images were processed and merged by using PHOTOSHOP (Adobe Systems, San Jose, CA). The analysis on colocalization of Mx1-YFP and nuclear bodies was determined in >350 nuclei. The statistical evaluation of the vicinity was carried out by Wilcoxon rank sum tests. The cell movement was corrected if necessary by using rigid registration (19). For single-particle tracking body positions were either defined by the brightest pixel or the center of mass by using IMAGEJ software (National Institutes of Health, Bethesda). Both methods gave the same results. The pair-wise motion correlation coefficients ρ were determined for all possible combinations. For body size calculation particle pixels were extracted by using TIKAL software (principles described in ref. 20). The velocity was determined for various time intervals ranging from 10 to 100 s. The mean square displacement (MSD) was calculated for each body and time point of the data set with

$$\text{MSD} = \langle d^2(\Delta t) \rangle = [d(t) - d(t + \Delta t)]^2 \quad [1]$$

and plotted as $\langle d^2 \rangle$ (μm^2) versus Δt (s) by using KALEIDAGRAPH (Synergy Software, Reading, PA). The value for the MSD at $\Delta t = 0$ is 0 with an uncertainty of $2.5 \times 10^{-3} \mu\text{m}^2$ as evaluated for 280 time points at 10-s intervals with fixed cells transfected with Mx1-YFP. The fitting of the MSD versus time was carried out by using Eqs. 3 and 4. For the average MSD plots 100 Mx1-YFP, 100 PML bodies, and 55 Cajal bodies were evaluated. For comparison of two fits, a normalized χ^2 was determined according to Eq. 2 with N being the number of time points, P the number of fit parameters, y_i the measured data values, σ_i the corresponding errors, and f_i the fit function values at the data points i with $1 \leq i \leq N$.

$$\chi^2 = \frac{1}{N - P} \sum_{i=1}^N \left(\frac{y_i - f_i}{\sigma_i} \right)^2 \quad [2]$$

Bodies were further tested for anomalous diffusion by using log-log plots (21). In the case of free diffusion, the result is a horizontal line. For anomalous diffusion, this plot has a slope of $\alpha = -1$. The slope was determined by using regression curve fitting, and the anomalous diffusion coefficient α was calculated. $\alpha > 0$ is considered as confined diffusion, $\alpha = 1$ indicates free diffusion, $\alpha < 1$ is interpreted as obstructed diffusion (21), and $\alpha > 1$ represents directed motion. Trajectories of random walks either measured or simulated were generated (for simulated data) and plotted on a square lattice, each site of which represents an image pixel, by using the software OBSTACLES written in our laboratory. To define the scale for simulated free diffusion the MSD of $\Delta t = 10$ s as observed for Mx1-YFP was extrapolated linearly. The trajectory coordinates for confined diffusion were taken from the measurements, whereas the values for free diffusion were generated by allowing a particle to jump from site to site with random direction. The degree of chromatin condensation during sodium azide treatment was determined by using correlation length analysis (22).

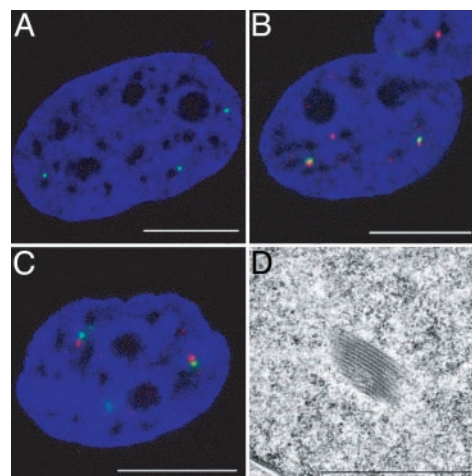


Fig. 1. Mx1-YFP colocalizes with nuclear bodies. Confocal images of Mx1-YFP (A), Mx1-YFP with PML bodies (B), and Mx1-YFP with Cajal bodies (C) are shown. Mx1-YFP is shown in green, PML and Cajal bodies in red, and 4',6-diamidino-2-phenylindole staining in blue. (D) Electron micrograph showing a Mx1-YFP body. (Scale bars: $10 \mu\text{m}$, A–C; $1 \mu\text{m}$, D.)

Results

Characterization of Mx1-YFP, PML, and Cajal Bodies. Upon low expression, Mx1-YFP formed bodies, which are $\approx 1 \mu\text{m}$ in size (Fig. 1A). On electron micrographs Mx1-YFP was found to have a crystalline organization. The bodies are built by a regular packing of filament-like structures (Fig. 1D). Interestingly, ultrastructural analysis revealed that the chromatin around the bodies has a distinct structure, which appeared to be less dense than the bulk chromatin (Fig. 1D). This was also observed for PML and Cajal bodies (data not shown). Although it cannot be excluded that this effect is caused by shrinkage during fixation, some fine texture in this region is visible on the original electron micrographs, arguing against an artifact of sample preparation. Fusions of Mx1-YFP bodies were not observed during time intervals up to 2.5 h probably because of their crystalline nature. In contrast, fusions of Cajal and PML bodies were observed within 16 min. Cajal body fusion had been demonstrated previously (23, 24), whereas PML body fusion has been controversially discussed (8, 25, 26). Fluorescence recovery after photobleaching experiments of Mx1-YFP bodies showed no recovery within 20 min, indicating the absence of a free nuclear Mx1-YFP pool that could exchange with the Mx1-YFP bodies (data not shown). In contrast, an exchange with a 50% recovery within few minutes was reported for some proteins of PML and Cajal bodies (25, 27–29). The missing antiviral activity and the crystalline structure make Mx1-YFP bodies a suitable reference system without bona fide biological activity. In our analysis, PML bodies were frequently located next to Mx1-YFP bodies (34% of all analyzed bodies, Fig. 1B), and Cajal bodies were also found preferentially next to them (50% of all bodies, Fig. 1C). This result is in agreement

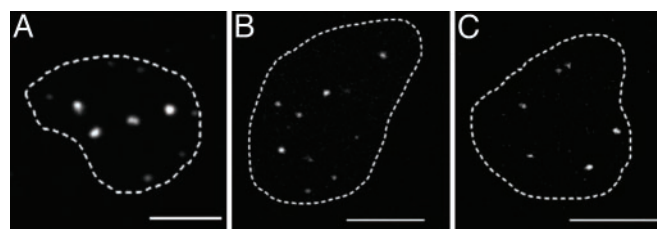


Fig. 2. *In vivo* images. Confocal sections of Mx1-YFP (A), PML bodies (B), and Cajal bodies (C) are shown. The nuclear shape is outlined by a dotted line. (Scale bars: $10 \mu\text{m}$.)

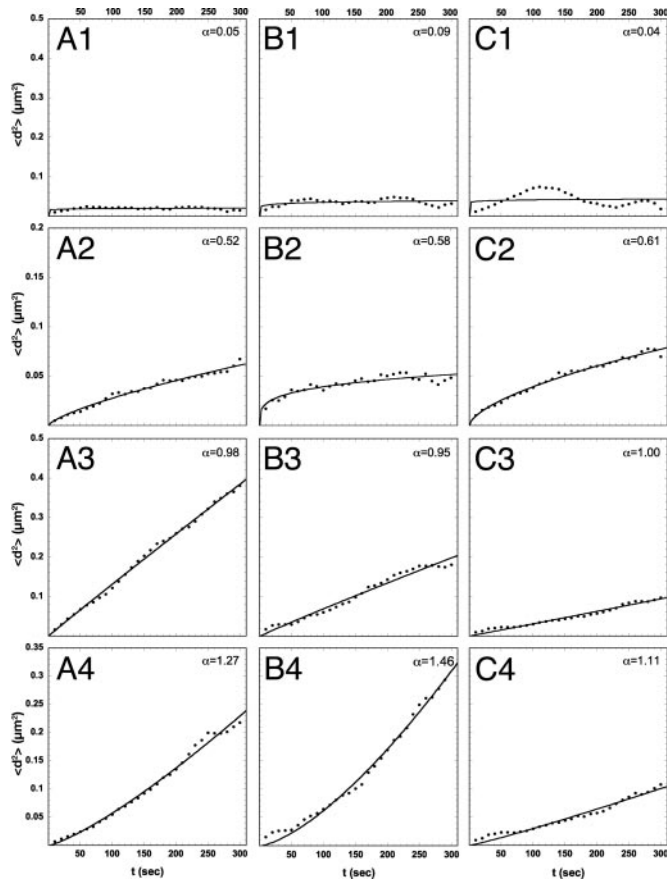


Fig. 3. A single nuclear body displays different types of motion over time. Confined, obstructed, and free diffusion as well as directed motion for individual Mx1-YFP (A1–A4), PML (B1–B4), and Cajal bodies (C1–C4) are shown. The respective α values for the classification are noted.

with the previously reported vicinity of Mx1 and PML bodies (30, 31). In contrast, the spatial relation of Mx1-YFP with nucleoli was significantly different because only 12% of Mx1-YFP bodies were found next to nucleoli.

General Features of Nuclear Body Movement. We expressed Mx1-YFP (Fig. 2A), coilin-GFP (Fig. 2B), or GFP-PML-III (Fig. 2C) in HeLa cells. The diffusion properties of the corresponding bodies were quantified by single-particle tracking. Analyzing data from 3D image stacks and 2D projections of these stacks led to the same diffusion properties, implying isotropic motion in all three directions. In such a case, the components in x , y , and z directions of the body movement can be treated as independent (see *Supporting Text*, which is published as supporting information on the PNAS web site), and the analysis of the diffusion behavior based on 2D image projections is correctly described by models for 2D motion (see *Supporting Text*).

All three types of bodies displayed an independent mobility as determined by pair-wise correlation analysis. Correlation coefficients of 0.07 ± 0.01 (PML bodies), 0.04 ± 0.02 (Cajal bodies), and 0.1 ± 0.02 (Mx1-YFP) on a scale from -1 (perfect anticorrelation) to 1 (perfect correlation) were determined. These values indicate that there was no correlation of body mobility. The average body size was similar for all body types (Mx1-YFP, $1.3 \pm 0.06 \mu\text{m}$; PML bodies, $1.2 \pm 0.07 \mu\text{m}$; and Cajal bodies, $1.0 \pm 0.04 \mu\text{m}$). On an average, 4 ± 1 Mx1-YFP particles, 14 ± 2 PML bodies, and 8 ± 3 Cajal bodies were found per nucleus. These sizes and numbers for PML and Cajal bodies are similar to those described in the literature (32, 33). The body velocity was found to be similar for the three

body types and displayed time dependence as expected for a nondirected movement. For a time interval of 10 s the velocity was $1.26 \mu\text{m}\cdot\text{min}^{-1}$ for Mx1-YFP, $1.56 \mu\text{m}\cdot\text{min}^{-1}$ for PML bodies, and $1.32 \mu\text{m}\cdot\text{min}^{-1}$ for Cajal bodies. To compare these values with the literature, the different time intervals of the measurements had to be considered, and values similar to those of previous studies were obtained: $0.1 \mu\text{m}\cdot\text{min}^{-1}$ versus $0.48\text{--}0.65 \mu\text{m}\cdot\text{min}^{-1}$ for Cajal bodies ($\Delta t = 180$ s) (23) and $2.8 \mu\text{m}\cdot\text{min}^{-1}$ versus $5.2 \mu\text{m}\cdot\text{min}^{-1}$ for PML bodies ($\Delta t = 5$ s) (8). A dependence of velocity on particle size was not observed for Cajal bodies with a correlation coefficient of 0.07, whereas Mx1-YFP ($\rho = 0.16$) and PML bodies ($\rho = 0.39$) showed a weak correlation. From a plot of the MSD versus time, four different types of mobility had been distinguished previously: confined diffusion, obstructed diffusion, free diffusion, and directed motion (34, 35). Our analysis of prolonged 4D data sets recorded for 16 min showed that a single Mx1-YFP (Fig. 3A1–A4), PML (Fig. 3B1–B4), or Cajal body (Fig. 3C1–C4) displayed periods of confined, obstructed, and free diffusion as well as directed motion during the observation time with a finite overall average step size. This behavior is consistent with statistical variations expected to occur for random Brownian motion. Accordingly, making use of the ergodic principle, the body displacement measured for a given time interval was averaged for all bodies of a given type to obtain the MSD plots shown in Fig. 4A–C.

The Moving Corral Model. The average mobility of PML and Cajal bodies as well as Mx1-YFP was different from free diffusion because no linear dependence of the averaged MSD versus time was observed (Fig. 4A–C). The MSD plots showed a high initial increase followed by a shallow apparently linear increase. It should be noted that this finding is in contrast to pure confined diffusion where the MSD reaches a plateau and to pure obstructed diffusion, which displays a nonlinear increase (21). Trajectories of Mx1-YFP were indistinguishable from those of PML and Cajal bodies (representative examples are shown in Fig. 8A, which is published as supporting information on the PNAS web site). The comparison with simulated free trajectories (Fig. 8B) clearly shows that the body movement is spatially restricted. Extending the theoretical framework from previous studies (35–37), we developed the following model (Fig. 5): the bodies are diffusing within a “corral” of accessible chromatin accounting for the high initial increase. These chromatin corrals can translocate within the nucleus, leading to the apparently linear dependence at later times. Thus, the measured diffusion of a body is composed of the body diffusion with constant diffusion coefficient (D_b) and chromatin motion characterized by constant D_c . This finding would be consistent with the electron micrographs, where the chromatin surrounding the bodies appeared to be less dense (see Fig. 1D for Mx1-YFP), allowing the bodies to move relatively fast within an area of a few hundred nanometers that is defined by the chromatin density distribution. An example for the restricted movement of an Mx1-YFP body in a putative chromatin corral is shown in Movie 1, which is published as supporting information on the PNAS web site. Using this model the average MSD plots fitted to an equation for diffusion of particles extending the theoretical framework developed by Saxton (36) and Saxton and Jacobson (38) (Fig. 4A–C, blue curves):

$$\text{MSD} = \langle r_c^2 \rangle \cdot \left(1 + \frac{4D_b t}{\langle r_c^2 \rangle} \right) \cdot \left[1 - \exp\left(- \frac{4D_b t}{\langle r_c^2 \rangle} \right) \right]. \quad [3]$$

The derivation of Eq. 3 is described in *Supporting Text* and yields the accessible chromatin space around the body r_c , the body D_b , and the chromatin D_c . The numbers for the D_b values represent lower limits because it is possible that a steeper initial increase of the MSD values would be observed if a time resolution shorter than $\Delta t = 10$ s is used. The D_b values (Table 1) obtained for PML ($D_b \geq 6.2 \times 10^{-3}$

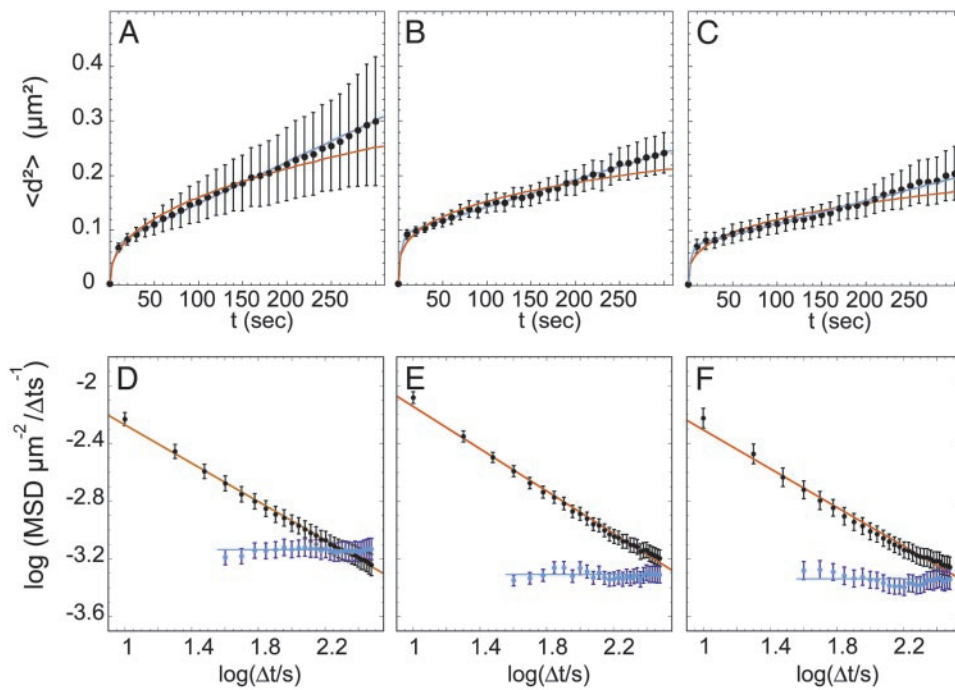


Fig. 4. Single-particle tracking analysis of nuclear bodies. Shown are average MSD plots for all Mx1-YFP (A), PML bodies (B), and Cajal bodies (C) examined. The fit for obstructed diffusion is shown in red, and the fit for diffusion of particles in corrals is shown in blue, both with weighted errors. The χ^2 values for the red and the blue fits are 0.34 and 0.27 for Mx1-YFP, 0.59 and 0.31 for PML bodies, and 0.47 and 0.28 for Cajal bodies. Average log-log plots for Mx1-YFP (D), PML bodies (E), and Cajal bodies (F) are shown. The normal log-log plots are shown in red with the α values 0.34, 0.27, and 0.33 for Mx1-YFP, PML, and Cajal bodies, respectively. The log-log plots with exclusion of D_b are shown in blue. The fit is a horizontal line obtained from the mean value of the curve points. The α values are accordingly 1.

$\pm 8.5 \times 10^{-4} \mu\text{m}^2\text{s}^{-1}$) and Cajal bodies ($D_b \geq 7.0 \times 10^{-3} \pm 1.7 \times 10^{-3} \mu\text{m}^2\text{s}^{-1}$) were slightly larger than the Mx1-YFP value ($D_b \geq 2.9 \times 10^{-3} \pm 4.0 \times 10^{-4} \mu\text{m}^2\text{s}^{-1}$). The r_c values are similar for all body types: Mx1-YFP, $0.28 \pm 0.03 \mu\text{m}$; PML bodies, $0.31 \pm 0.02 \mu\text{m}$; and Cajal bodies, $0.26 \pm 0.03 \mu\text{m}$. This finding supports the view that there is an accessible chromatin space of an average of 300 nm surrounding the bodies. The D_c values (Table 1) for the chromatin corrals were very similar for all three body types ranging from $1.1 \times 10^{-4} \pm 2.9 \times 10^{-5} \mu\text{m}^2\text{s}^{-1}$ to $1.8 \times 10^{-4} \pm 9.2 \times 10^{-5} \mu\text{m}^2\text{s}^{-1}$, which is consistent with the view that this component of

the movement reflects rearrangements of chromatin domains on a larger scale.

To examine whether bodies of different types were present with mobility significantly different from the average movement as depicted in Fig. 4, the r_c , D_c , and D_b values were calculated for all analyzed bodies individually. The resulting distributions for Mx1-YFP, Cajal, and PML bodies showed single peaks at almost identical positions (Fig. 6). No statistically relevant deviations that would be indicative of the presence of a species with higher or lower mobility were detected. This finding demonstrates that for all three nuclear body types only one population of bodies with respect to their diffusional properties was present. Within each class of bodies the values for D_c and D_b were uncorrelated with correlation coefficients between -0.1 and 0.1 .

Cajal bodies had been described to diffuse anomalously (7). For anomalous diffusion the MSD is no longer linear with time, but proportional to t^α with α being the anomalous diffusion coefficient and Γ a generalized transport coefficient according to Eq. 4:

$$\text{MSD} = 4\Gamma t^\alpha. \quad [4]$$

Eq. 4 was used to test whether our data can also be described by an anomalous diffusion model. The anomalous diffusion model did not result in a satisfactory fit of the data (Fig. 4 A–C, red graphs). Systematic deviations were observed at short times ($\Delta t < 50$ s) and longer times ($\Delta t > 250$ s). This qualitative difference between the two models was confirmed by a difference in the normalized χ^2 values for the two fits that is more than one order of magnitude larger for Eq. 4 and indicates that the fit to Eq. 3 is significantly better. A frequently used test for the anomalous diffusion behavior of a particle is the log-log plot (21), which yields a negative slope for anomalous diffusion (Fig. 4 D–F, red graphs). However, this type of analysis will not allow separating the two components for a biphasic diffusion behavior as proposed here. A separate plot of the slow component describing the corral motion can be obtained by subtracting the extrapolated value for $\Delta t = 0$ obtained from a linear fit of the data at $\Delta t \geq 40$ s. The resulting log-log plots demonstrate apparent free diffusion behavior for the slower component during the observation period (blue lines in Fig. 4 D–F). Thus, the overall

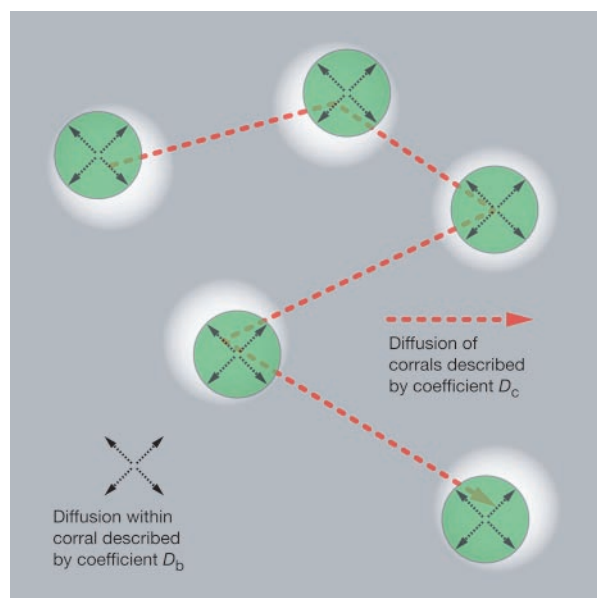


Fig. 5. Schematic illustration of nuclear body diffusion. The nuclear body is enclosed in a chromatin corral, defined by the chromatin accessibility in which they diffuse with D_b as demonstrated by the deformation of the chromatin. The chromatin corrals translocate within the nucleus with the D_c indicated by the red arrow.

the same values as those derived from the averaged trajectories. However, it should be noted that the finite dimensions of the cell nucleus will pose a limit to the maximum value of the MSD, which is not apparent on the time scale studied here. Our data can be described by a simple model, in which the bodies diffuse in and with a chromatin corral in the nucleus. The size of the corral is defined by the area of lower chromatin density around the bodies. Such a chromatin distribution is expected from its polymeric nature. In contrast to a liquid, polymers will not fill the available space near boundaries homogeneously unless a strong compressing force is present (42).

For Cajal bodies an association to small nuclear RNA, small nucleolar RNA, and histone genes has been reported (1–5), which suggests that Cajal bodies bind to specific chromatin loci. The binding of nuclear bodies to chromatin could contribute to the corraling, but it would have no effect on the long-range movements of corrals because of large-scale chromatin rearrangements. However, as Cajal bodies and Mx1-YFP bodies displayed essentially the same mobility and there is no evidence for a specific binding of Mx1-YFP bodies, any Cajal body interaction with chromatin is not detected in the analysis described here. This finding suggests that Cajal body binding to chromatin is transient, because otherwise the mobility should match with that of dense chromatin regions illustrated in Fig. 7. The model proposed here implies that any chromatin remodeling has a direct impact on body mobility. ATP depletion is likely to have complex effects on chromatin organization and dynamics. A marked decrease of chromatin mobility in yeast was reported after ATP depletion (39). We have also observed that ATP depletion can lead to chromatin condensation, which could increase the body mobility because of an extension of regions with lower chromatin density. On the other hand, nuclear bodies might become trapped in the condensed chromatin regions. Thus, it is difficult to assign the previously observed increased Cajal body mobility in HeLa (7) and decreased PML body mobility in baby hamster kidney cells (8) after ATP depletion simply to a direct energy-dependent binding affinity or transport mechanism. In addition, the response of Cajal and PML bodies to ATP depletion is likely to be cell line dependent because the fraction of PML bodies that moved over longer distances in an energy-dependent manner was not detected in HeLa cells (8). We therefore suggest that in energy depletion experiments of nuclear body mobility the effect of ATP depletion on chromatin structure and dynamics has to be considered.

Using different GFP-lac-repressor systems, rapid but locally restricted movements in mammalian cells as well as in yeast and *Drosophila* were shown to occur on a length scale of 0.4–0.5 μm (39, 43–46). This finding is in good agreement with the observed corral size (r_c) of $\approx 0.3 \mu\text{m}$ for all nuclear bodies determined here. Interestingly, in a recent paper very similar results were obtained from particle nanotracking (47). From an analysis of the dynamics of 100-nm diameter nanospheres nuclear microdomains with a mean size of $0.29 \pm 0.05 \mu\text{m}$ were identified. Thus, several lines of evidence support our finding that a chromatin space $\approx 0.3 \mu\text{m}$ is accessible for fast movements of nuclear bodies. Furthermore, the mean D value for the chromatin surrounding the nuclear bodies (D_c) of $1.36 \times 10^{-4} \mu\text{m}^2\text{s}^{-1}$ is identical to $D = 1.4 \times 10^{-4} \mu\text{m}^2\text{s}^{-1}$ for the movement of chromatin loci determined in the lac repressor system (45) and similar to values from 1.8 to $5.8 \times 10^{-4} \mu\text{m}^2\text{s}^{-1}$ measured for telomeres by using peptide nucleic acid probes (48). In summary, our analysis describes the movement of nuclear bodies as mostly determined by fluctuations of the chromatin density and large-scale movements of chromatin corrals within the nucleus. The artificial Mx1-YFP body introduced here showed mobility very similar to PML and Cajal bodies. This finding suggests that in our experimental system specific transport mechanisms for a certain type of body or body-specific chromatin interactions do not determine the movement of these bodies. The observed colocalization of bodies avoiding chromatin regions around the nucleolus indicates that only a subspace is accessible, consistent with the observation that the chromatin around the nucleolus is frequently more strongly condensed. These highly compacted chromatin loci had been frequently associated with silencing of biological activity. Other characteristic features of chromatin that lead to a preferred localization of nuclear bodies remain to be identified. Thus, concentrating certain transcription-related functions into nuclear bodies, which because of their physical nature are enriched in a more accessible chromatin environment, might be an effective mechanism to colocalize specific proteins with their target sites.

We thank K. Richter for the electron microscopy study; D. Spector and A. Lamond for critical reading of the manuscript; and D. Gerlich, S. Stertz, J. Fieres, J. Mattes, O. Haller, C. Cardoso, A. Möller, M. Reichenzeller, T. Knoch, A. Lamond, and D. Olins for reagents and support. This work was supported by Deutsche Forschungsgemeinschaft Grant Li406/5-3 and the Volkswagen Stiftung in the program Junior Research Groups at German Universities.

- Frey, M. R. & Matera, A. G. (1995) *Proc. Natl. Acad. Sci. USA* **92**, 5915–5919.
- Schul, W., van Driel, R. & de Jong, L. (1998) *Mol. Biol. Cell* **9**, 1025–1036.
- Jacobs, E. Y., Frey, M. R., Wu, W., Ingledue, T. C., Gebuhr, T. C., Gao, L., Marzluff, W. F. & Matera, A. G. (1999) *Mol. Biol. Cell* **10**, 1653–1663.
- Gall, J. G., Stephenson, E. C., Erba, H. P., Diaz, M. O. & Barsacchi-Pilone, G. (1981) *Chromosoma* **84**, 159–171.
- Kallen, H. G., Gall, J. G. & Murphy, C. (1991) *Chromosoma* **101**, 245–251.
- Shiels, C., Islam, S. A., Vatcheva, R., Sasieni, P., Sternberg, M. J., Freemont, P. S. & Sheer, D. (2001) *J. Cell Sci.* **114**, 3705–3716.
- Platani, M., Goldberg, I., Lamond, A. I. & Swedlow, J. R. (2002) *Nat. Cell Biol.* **4**, 502–508.
- Muratani, M., Gerlich, D., Janicki, S. M., Gebhard, M., Eils, R. & Spector, D. L. (2002) *Nat. Cell Biol.* **4**, 106–110.
- Gall, J. G. (2000) *Annu. Rev. Cell Dev. Biol.* **16**, 273–300.
- Negorev, D. & Maul, G. G. (2001) *Oncogene* **20**, 7234–7242.
- Lamond, A. I. & Sleeman, J. E. (2003) *Curr. Biol.* **13**, R825–R828.
- Spector, D. L. (2003) *Annu. Rev. Biochem.* **72**, 573–608.
- Haller, O. & Kochs, G. (2002) *Traffic* **3**, 710–717.
- Horisberger, M. A., Staeheli, P. & Haller, O. (1983) *Proc. Natl. Acad. Sci. USA* **80**, 1910–1914.
- Dreiding, P., Staeheli, P. & Haller, O. (1985) *Virology* **140**, 192–196.
- Möller, A., Sirma, H., Hofmann, T. G., Rueffer, S., Klimczak, E., Droge, W., Will, H. & Schmitz, M. L. (2003) *Cancer Res.* **63**, 4310–4314.
- Svitkina, T. M. & Borisy, G. G. (1999) *J. Cell Biol.* **145**, 1009–1026.
- Görisch, S. M., Richter, K., Scheuermann, M. O., Herrmann, H. & Lichter, P. (2003) *Exp. Cell Res.* **289**, 282–294.
- Fieres, J., Mattes, M. & Eils, R. (2001) in *Pattern Recognition DAGM 2001*, eds Radig, B. & Florczyk, S. (Springer, Berlin), Vol. 2191, pp. 76–83.
- Eils, R. & Athale, C. (2003) *J. Cell Biol.* **161**, 477–481.
- Saxton, M. J. (1994) *Biophys. J.* **66**, 394–401.
- Fejes Tóth, K., Knoch, T. A., Wachsmuth, M., Frank-Stöhr, M., Stöhr, M., Bacher, C. P., Müller, G. & Rippe, K. (2004) *J. Cell Sci.* **117**, 4277–4287.
- Platani, M., Goldberg, I., Swedlow, J. R. & Lamond, A. I. (2000) *J. Cell Biol.* **151**, 1561–1574.
- Boudonck, K., Dolan, L. & Shaw, P. J. (1999) *Mol. Biol. Cell* **10**, 2297–2307.
- Wiesmeijer, K., Molenaar, C., Bekeer, I. M., Tanke, H. J. & Dirks, R. W. (2002) *J. Struct. Biol.* **140**, 180–188.
- Eskiw, C. H., Dellaire, G., Mymryk, J. S. & Bazett-Jones, D. P. (2003) *J. Cell Biol.* **160**, 4455–4466.
- Sleeman, J. E., Trinkle-Mulcahy, L., Prescott, A. R., Ogg, S. C. & Lamond, A. I. (2003) *J. Cell Sci.* **116**, 2039–2050.
- Deryusheva, S. & Gall, J. G. (2004) *Proc. Natl. Acad. Sci. USA* **101**, 4810–4814.
- Handwenger, K. E., Murphy, C. & Gall, J. G. (2003) *J. Cell Biol.* **160**, 495–504.
- Chelbi-Alix, M. K., Pelicano, L., Quignon, F., Koken, M. H., Venturini, L., Stadler, M., Pavlovic, J., Degos, L. & de The, H. (1995) *Leukemia* **9**, 2027–2033.
- Engelhardt, O. G., Ullrich, E., Kochs, G. & Haller, O. (2001) *Exp. Cell Res.* **271**, 286–295.
- Monneron, A. & Bernhard, W. (1969) *J. Ultrastruct. Res.* **27**, 266–288.
- Zhong, S., Salomoni, P. & Pandolfi, P. P. (2000) *Nat. Cell Biol.* **2**, E85–E90.
- Simson, R., Yang, B., Moore, S. E., Doherty, P., Walsh, F. S. & Jacobson, K. A. (1998) *Biophys. J.* **74**, 297–308.
- Sako, Y. & Kusumi, A. (1994) *J. Cell Biol.* **125**, 1251–1264.
- Saxton, M. J. (1993) *Biophys. J.* **64**, 1766–1780.
- Saxton, M. J. (1995) *Biophys. J.* **69**, 389–398.
- Saxton, M. J. & Jacobson, K. (1997) *Annu. Rev. Biophys. Biomol. Struct.* **26**, 373–399.
- Heun, P., Laroche, T., Shimada, K., Furrer, P. & Gasser, S. M. (2001) *Science* **294**, 2181–2186.
- Kanda, T., Sullivan, K. F. & Wahl, G. M. (1998) *Curr. Biol.* **8**, 377–385.
- Schul, W., Groshout, B., Koberna, K., Takagaki, Y., Jenny, A., Manders, E. M., Raska, I., van Driel, R. & de Jong, L. (1996) *EMBO J.* **15**, 2883–2892.
- Grosberg, A. Y. & Khokhlov, A. R. (1994) *Statistical Physics of Macromolecules* (AIP Press, New York).
- Marshall, W. F., Straight, A., Marko, J. F., Swedlow, J., Dernburg, A., Belmont, A., Murray, A. W., Agard, D. A. & Sedat, J. W. (1997) *Curr. Biol.* **7**, 930–939.
- Vazquez, J. R., Belmont, A. S. & Sedat, J. W. (2001) *Curr. Biol.* **11**, 1227–1239.
- Chubb, J. R., Boyle, S., Perry, P. & Bickmore, W. A. (2002) *Curr. Biol.* **12**, 439–445.
- Abney, J. R., Cutler, B., Fillbach, M. L., Axelrod, D. & Scalettar, B. A. (1997) *J. Cell Biol.* **137**, 1459–1468.
- Tseng, Y., Lee, J. S., Kole, T. P., Jiang, I. & Wirtz, D. (2004) *J. Cell Sci.* **117**, 2159–2167.
- Molenaar, C., Wiesmeijer, K., Verwoerd, N. P., Khazen, S., Eils, R., Tanke, H. J. & Dirks, R. W. (2003) *EMBO J.* **22**, 6631–6641.

Supporting Text

The diffusion properties of the nuclear bodies were quantified by single particle tracking. Analyzing data from 3D image stacks and 2D projections of these stacks led to the same diffusion properties implying isotropic motion in all three directions. In such a case the components in the x , y , and z direction of the body movement can be treated as independent, and the analysis of the diffusion behavior based on 2D image projections is correctly described by models for 2D motion. This can be shown using the example of free diffusion: the solution of the diffusion equation in 3D

$$\frac{\partial c(x, y, z, t)}{\partial t} = D\nabla^2 c(x, y, z, t) \quad [1]$$

with the assumption to have a molecule with diffusion coefficient D at a position (x_0, y_0, z_0) at time 0 is the probability to find it at a position (x_1, y_1, z_1) at time t given by the Green's function

$$P_D^{(3D)}(x_1, y_1, z_1, t | x_0, y_0, z_0, 0) = (4\pi Dt)^{-3/2} \exp\left[-\frac{(x_1 - x_0)^2}{4Dt} - \frac{(y_1 - y_0)^2}{4Dt} - \frac{(z_1 - z_0)^2}{4Dt}\right]. \quad [2]$$

This is used to calculate the MSD according to

$$\text{MSD}^{(3D)} = \iiint dx_1 dy_1 dz_1 \iiint dx_0 dy_0 dz_0 W_D(x_0, y_0, z_0) \times P_D(x_1, y_1, z_1, t | x_0, y_0, z_0, 0) [(x_1 - x_0)^2 + (y_1 - y_0)^2 + (z_1 - z_0)^2] \quad [3]$$

where $W_D^{(3D)}(x, y, z) = \lim_{t \rightarrow \infty} P_D^{(3D)}(x, y, z, t | x_0, y_0, z_0, 0)$ is the equilibrium distribution, leading to the expected linear dependence of the MSD on time

$$\text{MSD}^{(3D)} = 6Dt. \quad [4]$$

In order to describe the projection of 3D data onto the x - y plane the integration is changed to

$$\text{MSD}^{(3\text{D,proj.})} = \iiint dx_1 dy_1 dz_1 \iiint dx_0 dy_0 dz_0 W_D(x_0, y_0, z_0) \times P_D(x_1, y_1, z_1, t | x_0, y_0, z_0, 0) [(x_1 - x_0)^2 + (y_1 - y_0)^2] \quad [5]$$

by deleting $(z_1 - z_0)^2$ and turns out to be the same as for true 2D diffusion:

$$\text{MSD}^{(3\text{D,proj.})} = \text{MSD}^{(2\text{D})} = 4Dt . \quad [6]$$

This follows from the definition of the Green's function as a normalized probability distribution and can be generalized to all processes where the Green's function can be factorized into terms each depending on only one spatial coordinate.

Because of its polymer properties, chromatin surrounding approximately spherical nuclear bodies in the cell nucleus is expected to show a gradual increase in density with increasing distance from the bodies, resulting in an apparent repulsive force on the bodies which may be approximated linearly. Diffusion in a corresponding isotropic harmonic potential

$U(x, y, z) = (x^2 + y^2 + z^2) / \langle r_c^2 \rangle / 6k_B T$ is an Ornstein-Uhlenbeck process and described by the Green's function (1)

$$P_D^{(3\text{D})}(x_1, y_1, z_1, t | x_0, y_0, z_0, 0) = \left(\frac{\pi \langle r_c^2 \rangle}{3} \right)^{-3/2} \left[1 - \exp\left(-2 \frac{6Dt}{\langle r_c^2 \rangle}\right) \right]^{-3/2} \times \exp\left(- \frac{3[x_1 - x_0 \exp(-6Dt/\langle r_c^2 \rangle)]^2 + 3[y_1 - y_0 \exp(-6Dt/\langle r_c^2 \rangle)]^2 + 3[z_1 - z_0 \exp(-6Dt/\langle r_c^2 \rangle)]^2}{\langle r_c^2 \rangle (1 - \exp[-2 \cdot 6Dt/\langle r_c^2 \rangle])} \right) \quad [7]$$

where $\langle r_c^2 \rangle$ is the long term MSD in 3D, or the correlation length of the space accessible to the bodies, or twice the squared radius of gyration of the chromatin corrals, respectively. This Green's function can be factorized as described above. Calculating the MSD projected to the x - y plane in analogy to the case of free diffusion gives

$$\text{MSD}^{(3\text{D,proj.})} = \langle r_c^2 \rangle \cdot \left[1 - \exp\left(-\frac{4D_b t}{\langle r_c^2 \rangle}\right) \right] \quad [8]$$

for confined body diffusion with a coefficient D_b , $\langle r_c^2 \rangle$ now being the long-term MSD in 2D.

In addition, when these chromatin corrals can translocate within the nucleus, one obtains the observed apparently linear dependence at later times within the time scales used in this study

$$\text{MSD}^{(3\text{D,proj.})} = \langle r_c^2 \rangle + 4D_c t \quad [9]$$

where D_c is the coefficient of chromatin diffusion. Deviations from linearity cannot be resolved under the experimental conditions of this study. This corral diffusion may include the motion of chromatin itself as well as the apparent motion of less dense regions caused by statistical polymer rearrangement, providing an accessible area of seemingly increasing size

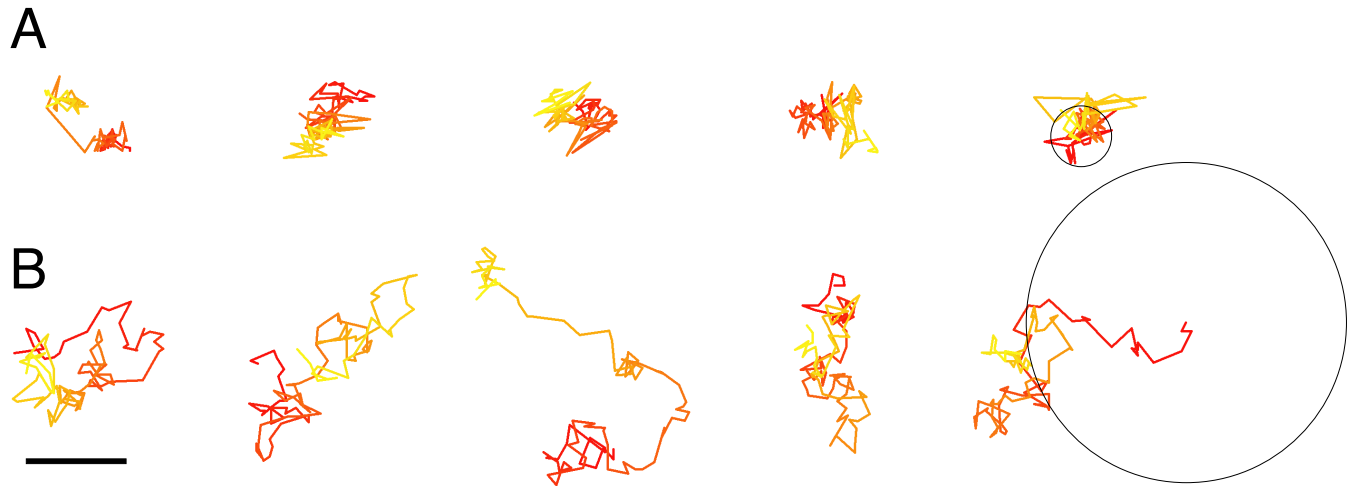
$$\langle r_c^2 \rangle \left(1 + \frac{4D_c t}{\langle r_c^2 \rangle} \right). \quad [10]$$

Thus, the measured trajectories are composed of the body diffusion with constant D_b and chromatin motion characterized by a constant D_c (Fig. 5). The two components are combined into an equation for diffusion of particles within a moving and/or increasing confinement that was fit to the average MSD plots (Fig. 4 A-C, blue curves):

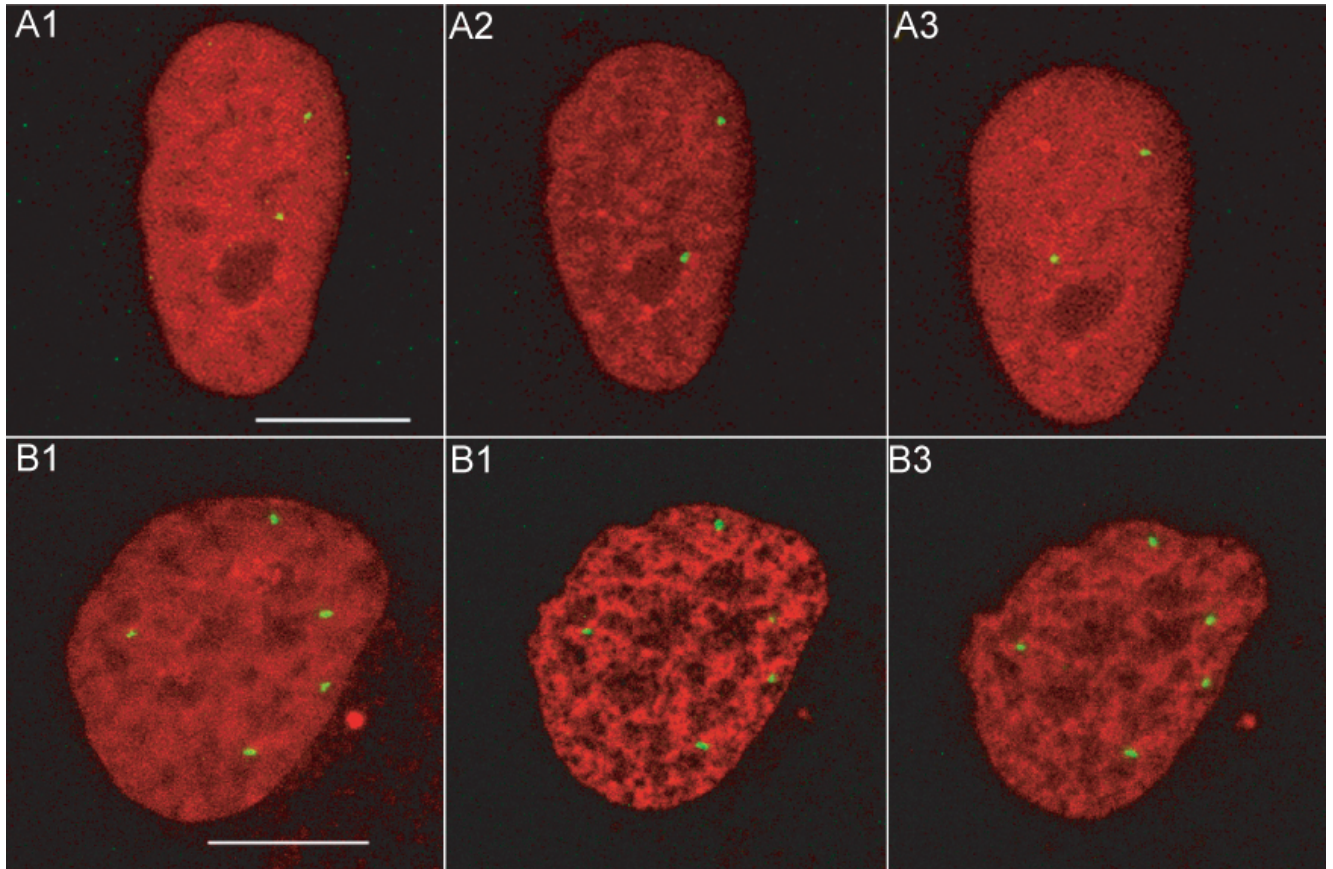
$$\text{MSD}^{(3\text{D,proj.})} = \langle r_c^2 \rangle \cdot \left(1 + \frac{4D_c t}{\langle r_c^2 \rangle} \right) \cdot \left[1 - \exp\left(-\frac{4D_b t}{\langle r_c^2 \rangle}\right) \right] \quad [11]$$

The binding of nuclear bodies to chromatin could contribute to the corralling effect, but is difficult to distinguish from purely steric confinement under the experimental conditions of this study.

1. Berne, B. J. & Pecora, R. (1976) *Dynamic Light Scattering* (Wiley, New York).



Supporting Fig. 8. Observed and simulated Mx1-YFP trajectories for 97 time steps of 10 s. The circle radii show the average distance between the body start (red) and end location (yellow) for this time period. (A) Measured trajectories for Mx1-YFP bodies. (B) Simulated trajectories for free random walks on a square lattice. The MSD of $D t = 10$ s for Mx1-YFP was extrapolated linearly. This result corresponds approximately to the value of diffusion coefficient D_b determined by fitting. (Scale bar: $1 \mu\text{m}$.)



Supporting Fig. 9. Chromatin condensation caused by azide treatment. (A) Maximum projections of Mx1-YFP particles in a SW13H2A-CFP cell nucleus: before treatment (A1), 22 min after addition of depletion buffer (A2), and 20 min after exchange to normal medium (A3) with a correlation length of 1.66, 0.85, and 1.6 m m, respectively. (B) Maximum projections of Mx1-YFP particles in a HeLa cell nucleus labeled in vivo with Hoechst 33342: before treatment (B1), 20 min after addition of sodium azide to the medium (B2), and 6 min after exchange to normal medium (B3). The correlation lengths are 1.01, 0.57, and 0.8 m m, respectively. The correlation lengths were calculated according to ref. 1. (Scale bars: 10 μ m.)